

---

This is an electronic reprint of the original article.  
This reprint may differ from the original in pagination and typographic detail.

Ding, Zhaodong; Tian, Zhongjian; Ji, Xingxiang; Wang, Dongxing; Ci, Xiaolei; Shao, Xuejun; Rojas, Orlando J.

## Cellulose-based superhydrophobic wrinkled paper and electrospinning film as green tribolayer for water wave energy harvesting

*Published in:*  
International Journal of Biological Macromolecules

*DOI:*  
[10.1016/j.ijbiomac.2022.12.122](https://doi.org/10.1016/j.ijbiomac.2022.12.122)

Published: 15/04/2023

*Document Version*  
Peer-reviewed accepted author manuscript, also known as Final accepted manuscript or Post-print

*Published under the following license:*  
CC BY-NC-ND

*Please cite the original version:*  
Ding, Z., Tian, Z., Ji, X., Wang, D., Ci, X., Shao, X., & Rojas, O. J. (2023). Cellulose-based superhydrophobic wrinkled paper and electrospinning film as green tribolayer for water wave energy harvesting. *International Journal of Biological Macromolecules*, 234, Article 122903. <https://doi.org/10.1016/j.ijbiomac.2022.12.122>

---

This material is protected by copyright and other intellectual property rights, and duplication or sale of all or part of any of the repository collections is not permitted, except that material may be duplicated by you for your research use or educational purposes in electronic or print form. You must obtain permission for any other use. Electronic or print copies may not be offered, whether for sale or otherwise to anyone who is not an authorised user.

# Cellulose-based superhydrophobic wrinkled paper and electrospinning film as green tribolayer for water wave energy harvesting

Zhaodong Ding<sup>1,2,4</sup>, Zhongjian Tian<sup>2</sup>, Xingxiang Ji<sup>1,2\*</sup>, Dongxing Wang<sup>3</sup>, Xiaolei Ci<sup>3</sup>, Xuejun Shao<sup>3</sup>, Orlando J. Rojas<sup>4,5</sup>

<sup>1</sup> Jiangsu Co-Innovation Center for Efficient Processing and Utilization of Forest Resources, College of Light Industry and Food Engineering, Nanjing Forestry University, Nanjing 210037, P.R. China

<sup>2</sup> State Key Laboratory of Biobased Material and Green Papermaking, Qilu University of Technology, Shandong Academy of Sciences, Jinan 250353, P.R. China

<sup>3</sup> Shandong Century Sunshine Paper Group Co., Ltd., Weifang 262400, P.R. China

<sup>4</sup> Bioproducts Institute, Department of Chemical and Biological Engineering, Department of Chemistry and Department of Wood Science, University of British Columbia, Vancouver, British Columbia V6T 1Z4, Canada.

<sup>5</sup> Department of Bioproducts and Biosystems, School of Chemical Engineering, Aalto University, Vuorimiehentie 1, FI-00076, Espoo, Finland

**ABSTRACT.** Water waves are viable low-carbon and renewable sources of power that can be optionally combined with triboelectric nanogeneration (TENG). Herein, we report on the synthesis of a TENG device based on green wrinkled paper tribolayers (W-TENG) assembled in grids (G-TENG) with channels that enable contact-separation modes involving metal balls that roll in phase with the waves. The W-TENG was prepared by spraying hydrophobic modified cellulose

nanofibrils on the surface of wrinkled paper. The paper's wrinkle wavelength and amplitude were adjusted by using a crepe blade at a given angle with respect to a drying cylinder, as well as the speed and torque. Coating was applied on the wrinkled paper using hyperbranched cationic polyethylenimine, obtaining polar hierarchical superhydrophobic cellulose micro/nanostructures, proposed as positive tribolayers with enhanced contact area and triboelectric density. The negative (biodegradable) tribolayers were prepared by electrospinning aqueous suspensions of polyvinyl alcohol and poly (ethylene oxide) reinforced with cellulose nanofibers. The triboelectric pair was shown to harvest energy from water waves, demonstrated in tests that highlighted the critical role of the wrinkling wavelength on energy output. The charge transfer by the W-TENG reached up to 40 nC in air and retained 27 nC under 85% relative humidity, ~5 and 7 times higher than those measured in planar TENG counterparts. A G-TENG array charging time (100- $\mu$ F capacitor) of ~188 s was measured when the voltage of the capacitor raised to ~1.5 V. Overall, we introduce a new, scalable TENG system that is demonstrated for its remarkable ability to harvest blue energy.

**Keywords:** Triboelectric nanogenerator, wrinkled cellulose, polarized hierarchical micro/nanostructure, grid-like array, water waves.

## 1. Introduction

The utilization of renewable and green energy has emerged as viable option towards the net-zero economy [1-3]. In this context, water wave energy is highly regarded for its broad applicability and sustainability . Global water wave power is estimated to exceed 2 TW [3, 4] but

such potential has not met the expectation even with state-of-the-art technologies designed for water wave energy harvesting. The main challenges in this field include the reliance on external power sources, the fabrication of high-quality materials, and their structural complexity [5-7]. More importantly, the conversion efficiency has been low and energy is produced randomly, associated with typical low-frequency waves [8, 9]. Hence, there is a need for low cost, structurally flexible and self-powered generators for water wave energy harvesting.

Triboelectric nanogenerators (TENGs) are efficient options to harvest random and irregular environmental mechanical energy, including that from water waves, wind as well as human motion. TENGs have attracted tremendous attention owing to their low cost, high efficiency, broad material selection, and flexible design [10-12]. The fundamental operating principle of TENG is the coupling effect of triboelectrification and electrostatic induction [13, 14]. TENGs' tribological materials with different polarities drive induced electrons in a circuit during periodic contact and separation, effectively converting mechanical energy into electricity [15-17]. Multiple TENG units can be integrated into a single TENG array to harvest water wave energy, under the principles of simple fabrication, low resistance to water wave motion and cost effectiveness [2, 3, 8, 12]. However, the tribolayers used so far in TENGs have been primarily derived from non-degradable and synthetic polymers, opening the opportunity for green TENG materials [18-21], including cellulose [22, 23]. Unfortunately, cellulose suffers from weak tribopositivity, which results in inferior generation of triboelectric charge, thereby reducing the TENG output [24, 25]. Furthermore, the hydroxyl groups of cellulose couple with water during collection of wave energy, leading to charge dissipation and hindering charge transfer [26]. For instance, ambient water vapor

can penetrate under the influence of temperature and humidity gradient and material expansion is expected to occur, which tends to impair friction and performance. Overall, increasing triboelectric charge density and moisture resistance are critical factors to ensure the collection and conversion efficiency of water wave energy via TENGs [27].

Based on the theory of triboelectric charge effect, the output of TENG is quadratically proportional to the charge density, which could be significantly improved by increasing the contact area and polarity of materials under contact [28-30]. To enhance the effective contact area, various layouts have been proposed, for instance, vertical stacking, stacked pendulum, origami, 3D-stacked, and aerogel structures [31, 32]. Nanoscale structure modifications and a proper selection of polarized materials are key to improve the frictional polarity [28, 33, 34]. Meanwhile, the introduction of superhydrophobic interfaces through surface modification can significantly expand the adaptability of TENGs for water wave energy harvesting [35-37].

Available cellulose-based TENG units and coupled TENG arrays so far have shown poor adaptability to water wave motion and output performance, limiting collection and conversion efficiency. Thus, there is a pressing need to improve the applicability and power generation capacity of sustainable TENG arrays to harvest water wave energy. Herein, we introduce a TENG grid (G-TENG) equipped with channels and multiple wrinkled paper-based TENG (W-TENG) that enable surface polarization according to the extent of surface wrinkling. Metal balls are used in the grid channels to eliminate the gravity imbalance of the G-TENG array and apply a load on each W-TENG unit, sufficiently and uniformly, to effectively convert wave energy into kinetic energy. Compared with a planar structure, the wrinkled structure is shown to enhance the frictional

contact area, by ~2.4 times. Silanized cellulose nanofibers (S-CNF) with high friction coefficient are used to coat the surface of W-CMF, yielding superhydrophobic and hierarchical micro/nanostructures that improve the moisture resistance and contact area. As a hyperbranched polymer with abundant electron-releasing amino groups, polyethyleneimine (PEI) is incorporated to further improve the friction polarity (forming a system that is therein referred to as PEI-S-CNF-W-CMF). Electrospinning is used to fabricate fiber webs of polyvinyl alcohol-cellulose nanofiber-poly (ethylene oxide) (PVA-CNF-PEO), used as negative triboelectric material. The electrospun film has a porous structure, which endows excellent biodegradability and friction properties. The designed W-TENG unit coupled with G-TENG is shown as an efficient option for water wave energy harvesting.

## **2. Results and discussion**

### *2.1 Structural design of W-TENG unit and coupled G-TENG array.*

According to the theory of the triboelectric charge effect, the performance of TENG is quadratically proportional to the triboelectric density, which can be enhanced by an increased contact area and polarity of the tribolayers [19, 25, 26, 38]. Previous reports have demonstrated that wrinkled structures optimize the utilization of space and produce a large contact area for energy harvesting. For this purpose, wrinkled papers were produced following dry-creping, Fig. 1a, under a difference of paper velocity (lower outlet speed compared to the entrance speed) [39, 40], where the amplitude and wavelength of the wrinkles are controlled by the angle of the scraper

and the speed difference [41, 42]. As such, the contact area of the W-CMF increases from 6 to 14.4 cm<sup>2</sup> as the wrinkling wavelength decreases from 4.6 to 1.4 mm (Fig. 1b). In the case of similar wrinkling amplitudes, the reduction in wavelength increases the relative contact area [15, 43].

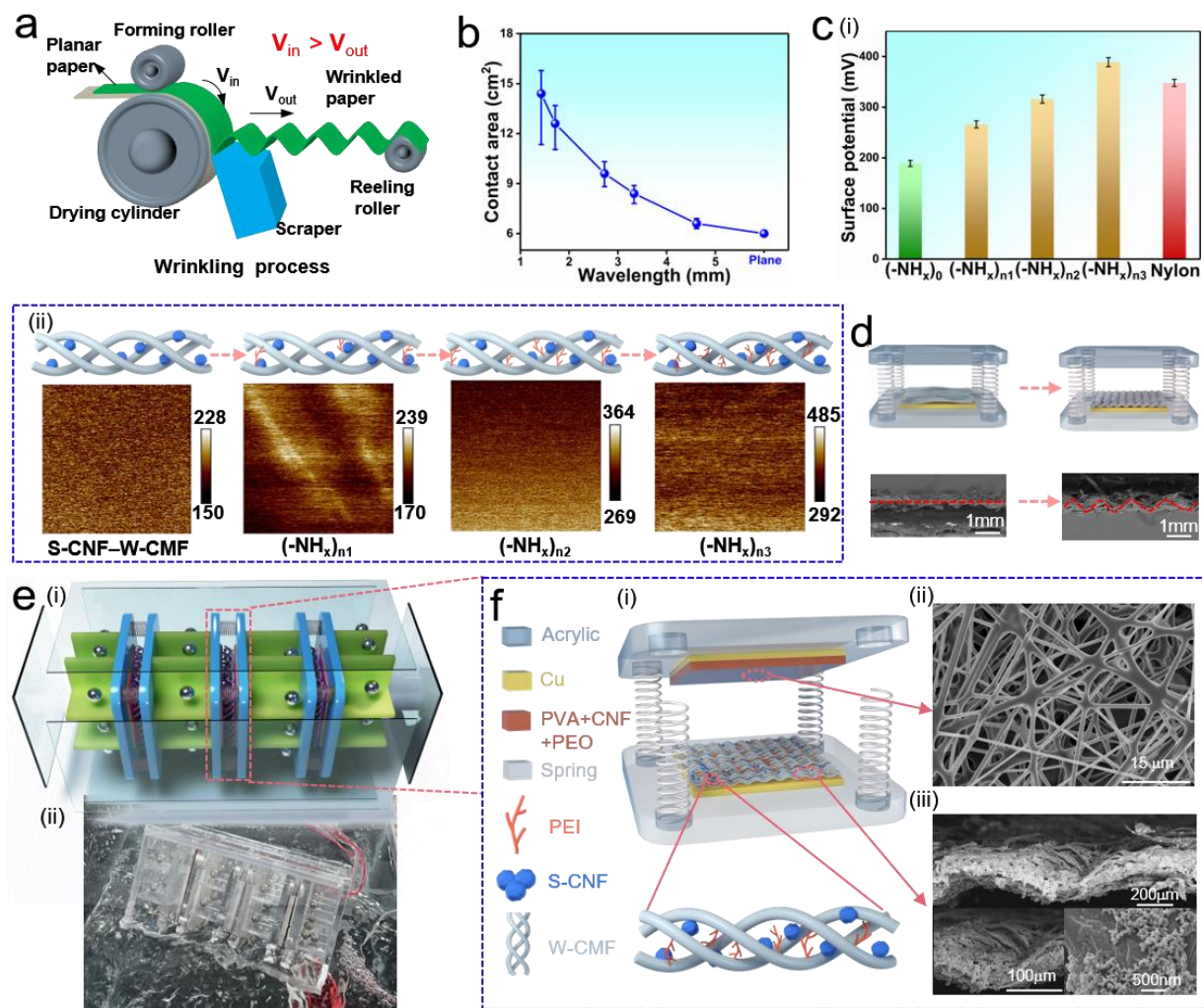


**Fig. 1.** Design of the wrinkled paper-based triboelectric nanogenerator (W-TENG) and grid of triboelectric nanogenerator (G-TENG). (a) Schematic of the paper creping process to generate the tribolayers, W-CMF. (b) Relative contact area at different wrinkling degrees. (c) Surface potential of different number density of  $-NH_x$ . (d) Schematic representation of W-TENG at different wrinkling degrees. (e-i) Schematic representation and (e-ii) photograph of a G-TENG array with three units. (f-i) Schematic representation of a PEI-S-CNF-W-CMF W-TENG unit. (f-ii)

Scanning electron microscopy (SEM) of the web produced with polyvinyl alcohol–cellulose nanofiber–poly (ethylene oxide) (PVA–CNF–PEO), and (f-iii) the PEI–S–CNF–W–CMF paper.

Nanoscale materials with high friction coefficients have been used as fillers for physical compounding with cellulose, e.g., to introduce new functionalities and enhance charge attraction or charge trapping abilities [44]. Tetraethyl orthosilicate and dodecyltriethoxysilane were coated on the surface of CNF (S–CNF) to form a W–CMF construct with a hierarchical micro/nanostructure that is superhydrophobic. Such effect is expected to improve the moisture resistance, while enhancing contact area and friction polarity of the tribolayer (Fig. 1f-iii). Furthermore, the ability to gain or lose charge could be controlled by modifying the functional groups on the cellulose surface [45–47]. To verify the effect of chemical modification on friction polarity, the S–CNF–W–CMF material was further modified with PEI at given concentrations, installing different number of electron-donor amino groups. A schematic representation of the PEI modification and change in surface potential is shown in Fig. 1c. The number of amino groups contacting the PVA–CNF–PEO surface increases with the concentration of PEI, generating more surface charges. The increase in the number of  $-NH_x$  groups resulted in an increase in the surface potential, from 189 mV to 388 mV. The obtained PEI–S–CNF–W–CMF assembly acted as friction material with strong electron contribution compared to S–CNF–W–CMF. In addition, the surface potential of PEI–S–CNF–W–CMF was higher than that of nylon (surface potential of 351 mV). Herein, PEI–S–CNF–W–CMF W–TENG with different wrinkling degrees were designed (Fig. 1d).

The structure of the G–TENG array, with internal grid channels comprising W–TENG units and

metal balls is schematically shown in Fig. 1e-i. The G-TENG array with three units were used to collect energy from water waves, Fig. 1e-ii. Each channel, consisting of nine square grids, supported high-strength stainless steel balls (Type 304 material, 6.8 g) with good nonmagnetic, antirust, and anticorrosion properties. This setup eliminates the gravity imbalance and facilitates sufficient contact between the metal balls and the W-TENG unit.

In constructing the TENG, we selected a couple of suitable friction materials with large electron affinity difference [48-50]. As shown in Fig. 1f, PEI-polarized and S-CNF-coated W-CMF (PEI-S-CNF-W-CMF) with a hierarchical micro/nanostructure were used as the positive friction material. Electrospun PVA-CNF-PEO = with both excellent biodegradability and friction properties served as negative triboelectric material (Fig. 1f-ii). Acrylic was used as the substrate, and a spring was used as support material.

## *2.2 PEI-S-CNF-W-CMF and PVA-CNF-PEO pairs.*

To investigate the influence of wrinkling degree on the contact area, we prepared W-CMF with wavelengths varying from 1.4 to 4.6 mm (Fig. 2a). A reduced wavelength, from 4.6 to 1.4 mm, produced an increased contact area, from 6 to 14.4 cm<sup>2</sup>. S-CNF-coated and PEI-modified W-CMF displayed a hierarchical micro/nanostructure and high surface potential and were synthesized using physical doping and chemical modification, respectively (Fig. 2b). Uniform and well-dispersed cellulose nanofibers (CNF) were prepared using enzymatic pretreatment and mechanical deconstruction. S-CNF modified with SiO<sub>2</sub> were produced by two-step silanization of CNF. The rough surface nanostructure of CNF was produced by cleaving the alkoxy bond in Si[OCH<sub>2</sub>CH<sub>3</sub>]<sub>4</sub>, generating SiO<sub>2</sub>, which was arranged around the cellulose chains (Fig. S1). The first step in the

process included hydrolysis of  $\text{Si}[\text{OCH}_2\text{CH}_3]_4$  to form monosilicic acid and ethanol. Subsequently, a condensation reaction took place between monosilicic acid and monosilicic acid or between monosilicic acid and ethyl orthosilicate to generate Si–O–Si bonds. The resulting oligomer further underwent polymerization to form a long-chain, stable  $\text{SiO}_2$  structures. A chemical group with a low surface energy was introduced through grafting of  $\text{CH}_3[\text{CH}_2]_{11}\text{Si}[\text{OCH}_2\text{CH}_3]_3$  on the surface of  $\text{SiO}_2$  (Fig. S2).

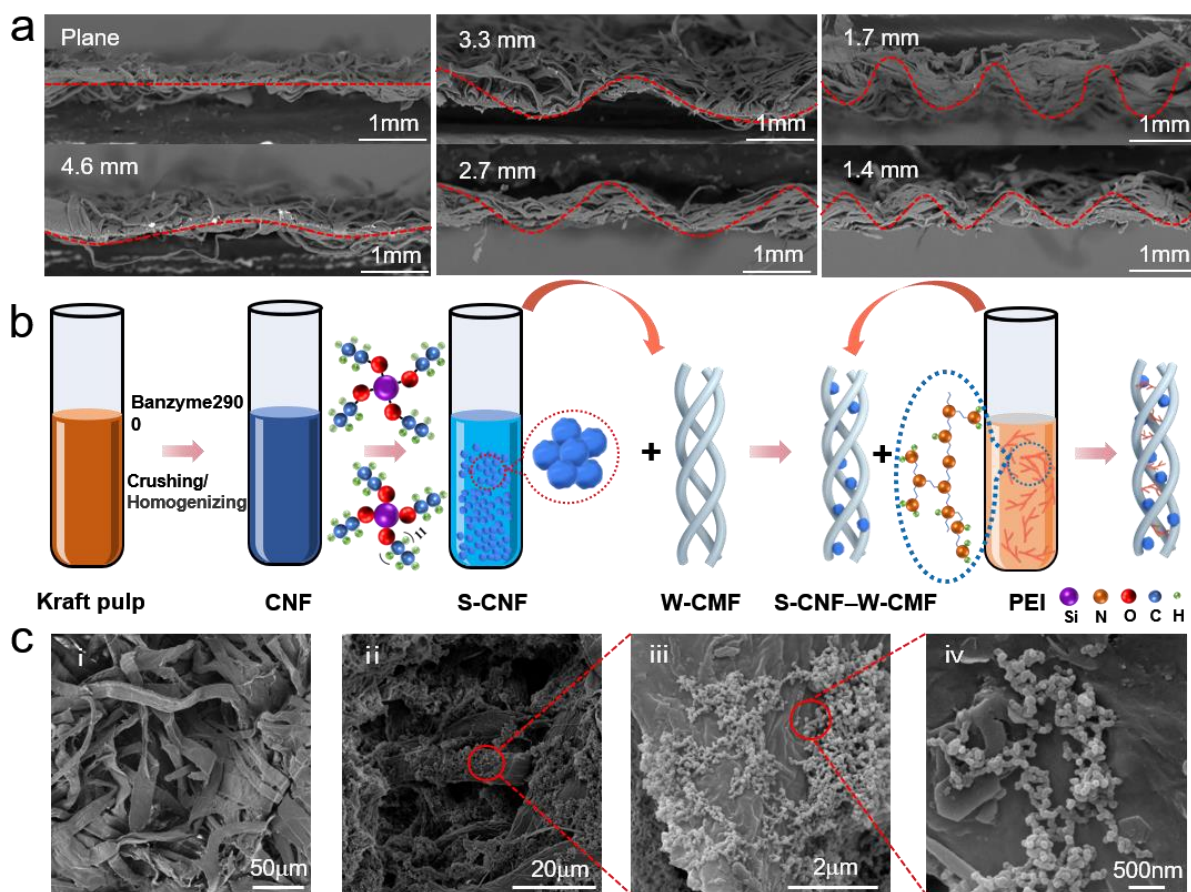


**Fig. 2.** Formation mechanism and characterization of PEI-S-CNF-W-CMF. (a) Cross-sectional SEM topography of W-CMF of different wrinkling wavelengths: 4.6, 3.3, 2.7, 1.7, and 1.4 mm. (b) Schematics of the preparation process of the micro/nanostructure of PEI-S-CNF-W-CMF. (c) SEM topography of W-CMF and PEI-S-CNF-W-CMF.

The oligomers generated at the end of reaction underwent further polymerization, grew along the direction of the Si–O–Si bonds, and formed hydrophobic alkyl chains on the surface of SiO<sub>2</sub>, which, in turn, endowed the surface of CNF with superhydrophobic properties. Consequently, SiO<sub>2</sub> nanostructures were produced, and long carbon chain groups of low surface energy were introduced on the S-CNF surface (Fig. S3). During polarization modification, the amino groups of PEI were combined with the hydroxyl group of CNF–W-CMF through hydrogen bonding, which enhanced the triboelectric charge density of PEI–S-CNF–W-CMF (Fig. S4). The hierarchical micro/nanostructure of the as-fabricated PEI–S-CNF–W-CMF is shown in Fig. 2c and the PEI polarization modification of W-CMF was analyzed (Fig. S5). X-ray photoelectron spectroscopy (XPS) and Fourier transform infrared spectroscopy (FTIR) were used to determine the chemical structures of PEI–W-CMF, proving PEI was successfully grafted on W-CMF.

The preparation process, photos and thickness of PVA–CNF–PEO films are shown in Fig. S6. It can be observed that void structures are formed between the micro/nano nanofibers, and the water contact angle of the esterified PVA–CNF–PEO film was 109° at 2 min (Fig. S7), which prevented water vapor from diffusing to W-TENG.

### *2.3 Working mechanism of the W-TENG unit.*

The working mechanism of TENG involves a combination of triboelectrification and electrostatic induction that converts external mechanical energy into electrical energy [32, 51]. An electron cloud model is proposed to explain the contact electrification process of W-TENG (Fig. S8) [52]. COMSOL was employed to simulate the potential distribution of the contact-separation mode-based W-TENG (Fig. 3a). The structure of the W-TENG is shown in Fig. 3b [52]. PEI-S-

CNF-W-CMF and PVA–CNF–PEO were the positive and negative tribolayers, respectively. When the two materials were in contact, the transferred charges trapped in the surface states compensated each other, and therefore, no current flow occurred in the external circuit (Fig. 3b-i). Subsequently, during the separation process of the tribolayers, the surface transfer charge caused a shift in the Fermi level of the corresponding Cu electrodes (Fig. 3b-ii). Hence, a potential was generated between the two Cu electrodes due to electrostatic induction, which drove current flow. When the two friction materials were separated, the Fermi level difference in the two Cu electrodes was fully balanced by the transferred electrons and no current flow occurred through the external circuit (Fig. 3b-iii). Eventually, the two materials come in contact, and the Fermi-level difference between Cu electrodes is reduced. Afterward, the current flow go back until the two tribolayers return to full contact (Fig. 3b-iv). Hence, an alternating current is generated by pressing and releasing the cyclic external load applied to the W-TENG (Fig. 3c).

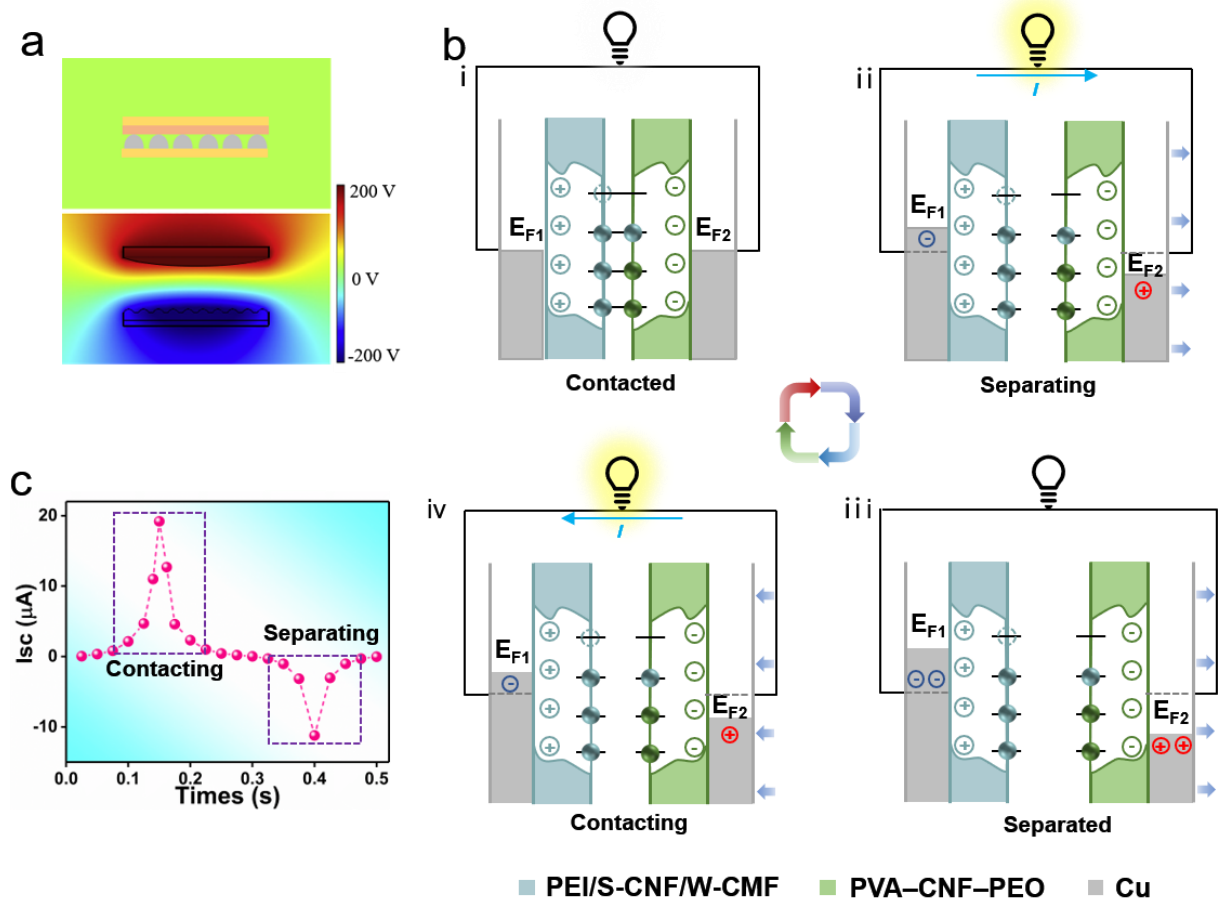


**Fig. 3.** The working mechanism of a W-TENG unit. (a) Numerical calculations on the potential distribution at different working states of W-TENG. (b) Electrostatic induction process of a contact-separation mode-based W-TENG. (c) Current output under one cycle of contact and separation of W-TENG.

#### 2.4 Energy application and moisture resistance of W-TENG unit.

Cellulosic paper is not an ideal tribolayer material given its planar geometry, relatively low friction and high hydrophilicity. Paper does not generate charges nor store energy under water wave motion, preventing the collection and conversion efficiency of a TENG [20, 24]. Therefore, a wrinkled structure based on W-CMF was designed to increase the triboelectric charge density by enhancing the effective contact area (Fig. 4a). A TENG with a planar CMF (6 cm<sup>2</sup>) produced a

voltage of 21 V when pressed and released at 2 Hz with a force of 10 N. Conversely, W-CMF (14.4 cm<sup>2</sup>) based W-TENG exhibited a voltage of 55 V, a 162% increase. Meanwhile, the transferred charge was enhanced, from 8 to 17 nC, as well as the current, from 6 to 14 μA (a 113% and 142% increase, respectively) (Fig. 4c).

To increase the moisture resistance, contact area, and friction polarity of W-TENG, S-CNF was coated with SiO<sub>2</sub>, used as a construct of unique hierarchical micro/nanostructure. The material was superhydrophobic and PEI was grafted to further increase the surface polarity (Fig. 4b). When the -NH<sub>x</sub> content of the polarized material coated by S-CNF was high (x=n3), the transferred charge increased from 17 to 41 nC, a 141% increment compared to that of W-CMF (Fig. 4d). Simultaneously, the voltage increased from 55 to 94 V, as well as the current, from 14 to 19 μA (71% and 40% higher, respectively) (Fig. S9).

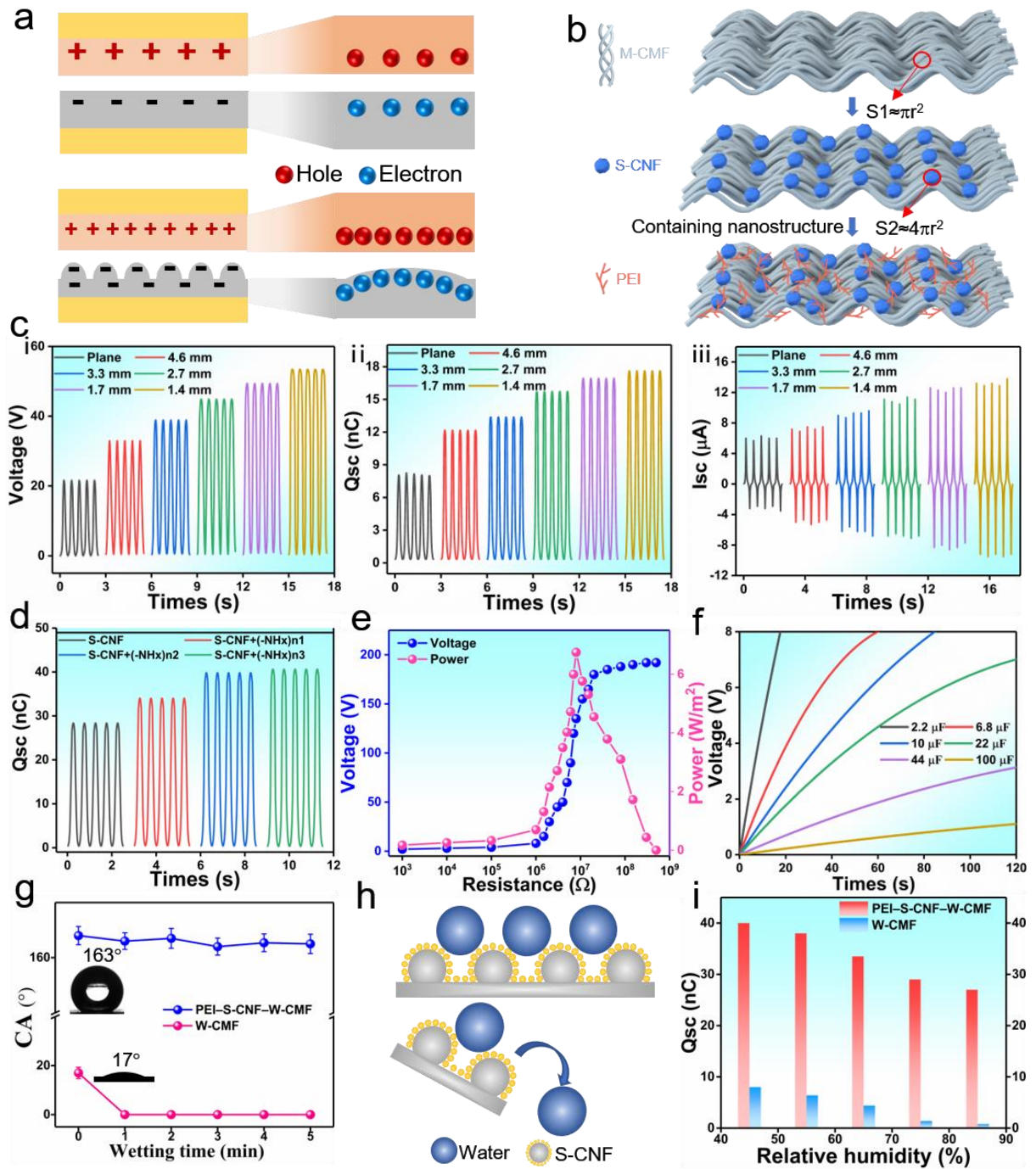


**Fig. 4.** Energy applications and moisture resistance of W-TENG unit (a) Schematic diagram of the relationship between triboelectric charge density and surface roughness. (b) Influence mechanism of output performance. (c-i) Output voltage, (c-ii) transferred charges, and (c-iii) current based on the W-CMF with varying wrinkling degrees, ranging from 1.4 to 4.6 mm. (d) Transferred charges of the W-TENG based on PEI-S-CNF-W-CMF with different amounts of -NHx. (e) The

relationship between output voltage and power of W-TENG and external load resistance. (f) Voltage of the various capacitors charged by the W-TENG. (g) Hydrophobic capacity and hydrophobic stability. (h) Schematic of superhydrophobic systems. (i) Dependence of transferred charges on relative humidity.

Systematic experiments were carried out to explore the effect of operating frequency and contact force on the output power of the W-TENG (Fig. S10). The voltage and transferred charges showed no significant changes as the operating frequency was increased. This is explained by the saturation of tribocharges on the PEI-S-CNF-W-CMF surface. However, the current increased from 19 to 31  $\mu\text{A}$  when the frequency increased from 2 to 5 Hz, which is consistent with a current that depend on the surface charge density and the charge transfer period. The voltage, transferred charges and current were positively related to the applied force. The voltage, transferred charges, and current increased from 94 V, 41 nC, and 19  $\mu\text{A}$  to 191 V, 73 nC, and 36.1  $\mu\text{A}$ , respectively, when the operating force changes from 10 to 50 N. This result is attributed to the increased contact area between the two tribosurfaces as the applied force increased.

Charged by a W-TENG unit operated under 2 Hz and 10 N, the output power of the W-TENG was studied using a resistance as the external load for environmental mechanical energy conversion. The voltage increased with the enhanced load resistance and the instantaneous maximum power reached 6.7  $\text{w}/\text{m}^2$  with a load resistance of  $8 \times 10^6 \Omega$  (Fig. 4e). Capacitors serve as one of the fundamental components of various electronic products, which can be used to assess the output performance of the W-TENG unit by charging capacity. The results of Fig. 4f indicate that the voltages of the 2.2 and 100  $\mu\text{F}$  capacitors could attain 8 and 1.1 V within 120 s, respectively,

displaying excellent charging performance.

To verify the superhydrophobic ability and stability of PEI-S-CNF-W-CMF, the change in the water contact angle (CA) was investigated. We note that the initial CA of W-CMF was  $17^\circ$ , which decreased to  $0^\circ$  in 1 min. While W-CMF is hydrophilicity due to a large number of hydroxyl groups on their surface (Fig. 4g). The initial CA of CMFPEI-S-CNF-W-CMF was  $163^\circ$ , and presented negligible changes with time. Based on the Cassie-Baxter theory, superhydrophobicity is mainly derived from the combination of a  $\text{SiO}_2$  nanostructure with low surface energy, long carbon chain groups, and air trapped in the grooves, between  $\text{SiO}_2$  when water droplets fall on the surface of PEI-S-CNF-W-CMF (Fig. 4h). The water droplets touch the uneven top, forming a water-air interface, and then the friction material is not penetrated by the water droplets. To verify the moisture resistance of the W-TENG, transferred charges were determined to investigate the dependence of the performance of W-TENG on relative humidity (Fig. 4i). The transferred charges showed negative changes as the relative humidity increased due to the dissipation of triboelectric charges on the PEI-S-CNF-W-CMF and W-CMF surfaces [53]. When the relative humidity reaches 85%, the transferred charge of W-CMF decreased from 8 to 0.79 nC, and the transferred charge of PEI-S-CNF-W-CMF decreased from 40 to 27 nC. These results demonstrated the high moisture resistance of PEI-S-CNF-W-CMF with a superhydrophobic interface, which contributed to the improvement of the W-TENG's stability under harsh humid conditions. Long carbon chain with low surface energy and 0D  $\text{SiO}_2$  with nanostructure formed a water-air interface between the water droplets and the surface of PEI-S-CNF-W-CMF, making the positive friction material impermeable to water penetration. Moreover, when the negative PVA-CNF-PEO tribolayer was

pressed against the positive PEI–S–CNF–W–CMF friction material with the superhydrophobic interface, led to a discharge of the surface water droplets because the nanoscale rough surface weakens the adhesion of the water droplets [54].

### *2.5 Application of a G-TENG array in water-wave energy harvesting.*

To investigate the TENG application for wave energy harvesting in large scale, the grid-like G-TENG array with internal channels was put together with three W-TENG units and 27 metal balls (Fig. 5a). W-TENG unit with polarized hierarchical micro/nanostructure had a high triboelectric charge density and moisture resistance. The metal balls in the grid channels applied an impact force to each W-TENG unit and converted the water-wave energy into kinetic energy. The circuit diagram of the array showed that the connection of every unit was parallel and the output was rectified (Fig. 5b).

The effects of the unit number of the G-TENG array and the water-wave frequency are addressed next. The output current increased when the unit number rose from 1 to 3, and the array with three units had the highest value, 28  $\mu\text{A}$  (Fig. 5c). With an increased frequency of the water wave, from 0.5 to 2.5 Hz, the values of output current initially increased and gradually decreased, exhibiting the peak value of 46  $\mu\text{A}$  at 2.0 Hz (Fig. 5d). The high water-wave frequency accelerated the motion period of the TENG, resulting in an incomplete reciprocating motion of the metal balls in the inner grid, which reduced the impact force exerted on the W-TENG unit.

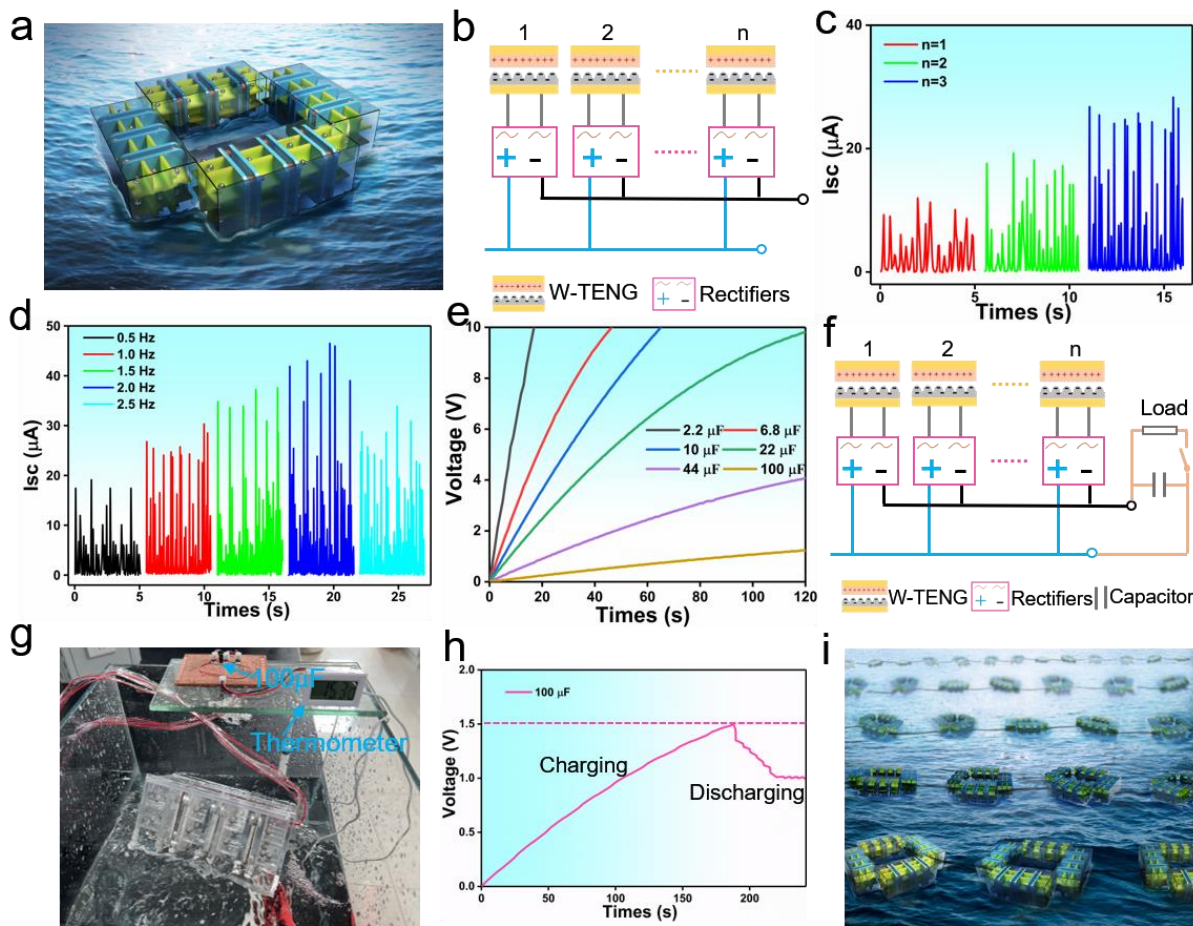


**Fig. 5.** Application of G-TENG array in water-wave energy harvesting. (a) Schematics of the G-TENG array for harvesting water-wave energy. (b) Schematics of the rectifier circuit for the G-TENG array. (c) The output current of the G-TENG array with different numbers of units ranging from 1 to 3 at 1 Hz. (d) The output current of the G-TENG array with three units at different frequencies ranging from 0.5 to 2.5 Hz. (e) Voltages of various capacitors charged by the G-TENG array with three units at 2 Hz. (f) Schematics of the circuit for powering the thermometer. (g) Photograph of water temperature measurement powered by the G-TENG array. (h) Charge–discharge process for a 100- $\mu$ F capacitor to power the thermometer. (i) Imaginary picture of future G-TENG arrays toward massive ocean energy harvesting.

The G-TENG array efficiently charged various capacitors, which in turn powered various small electronic devices, such as micro-transmission modules and sensors (Fig. 5e). Herein, an

application of the array to power a thermometer was shown to measure water temperature. The circuit schematic for powering the thermometer is shown in Fig. 5f, indicating that each unit was rectified and subsequently connected in parallel to power a 100- $\mu$ F capacitor. The thermometer started displaying the right temperature of water when the voltage increased to  $\sim 1.5$  V (Fig. 5g). The charging time of a 100- $\mu$ F capacitor using the G-TENG array was  $\sim 188$  s (Fig. 5h). An efficient method for large-scale massive blue energy harvesting can be expected by using parallel G-TENG arrays (Fig. 5i).

### **3. Conclusion**

In summary, we assembled a TENG grid (G-TENG) composed of channels supporting metal balls that roll in phase with water waves, contacting wrinkled paper-based TENG units (W-TENG) and converting the kinetic energy into electrical currents. The transferred charges in the W-TENG units reached up to 40 nC in air and retained 27 nC under 85% relative humidity,  $\sim 5$  and 7 times higher than those generated by planar TENG, respectively. The charging time of G-TENG array for a 100- $\mu$ F capacitor is  $\sim 188$  s when the voltage of the 100- $\mu$ F capacitor rose to about 1.5 V, which was driven by the water waves. The design of the W-TENG unit and coupled G-TENG array is an efficient option for water wave energy harvesting.

### **4. Experimental section**

*Materials:* Kraft pulp was sourced from a paper mill (Shandong, China). Endoglucanase (Banzyme 2900) was provided by UPM-Kymmene Co., Ltd (Jiangsu, China). Commercially

available tetraethyl orthosilicate ( $\text{Si}[\text{OCH}_2\text{CH}_3]_4$ ) and dodecyltriethoxysilane ( $\text{CH}_3[\text{CH}_2]_{11}\text{Si}[\text{OCH}_2\text{CH}_3]_3$ ) were obtained from Aladdin (Shanghai, China). Polyvinyl alcohol (PVA), poly (ethylene oxide) (PEO) and polyethyleneimine (PEI) were purchased from Aladdin (Shanghai, China). The copper tape, acrylic, and spring were purchased from Meitai Flagship Store (Jiangsu, China).

*Fabrication of W-CMF:* The authors, with Asia Symbol (Shandong) Pulp & Paper Co., Ltd, assembled a four-point synchronous transmission system to produce paper with different degrees of wrinkling (W-CMF). The load distribution considered the speed and torque, ensuring speed synchronization of the master and slave transmission units, and accurately controlling the torque and angle difference.

*Preparation of S-CNF:* Kraft pulp fibers were pretreated with enzymes and then mechanically disintegrated using an ultrafine particle grinder to decrease the size of cellulose fiber into micro/nanofibrils (CNF). CNF was obtained by mechanically treating 1 wt% suspension of micro/nanocellulose with an M-110EH-30 microfluidizer (MA, USA).  $\text{Si}[\text{OCH}_2\text{CH}_3]_4$  (8 ml) and  $\text{CH}_3[\text{CH}_2]_{11}\text{Si}[\text{OCH}_2\text{CH}_3]_3$  (4 ml) were added to 100 g of absolute ethanol and stirred uniformly. Subsequently, the ethanol-washed CNF was added to the reaction system in a sonicator for 4 h. Finally, S-CNFs were obtained via centrifugation and washed with absolute ethanol.

*PEI-S-CNF-W-CMF tribolayer:* The S-CNF-W-CMF was prepared by spraying S-CNF with (1 %wt) on the surface of W-CMF. PEI-S-CNF-W-CMF was prepared by coating the surface of S-CNF-W-CMF with PEI via S-CNF-W-CMF evaporation of free water from the PEI solution. 2, 4, and 6 g of PEI were dissolved in 48, 46, and 44 g of purified water and mixed at room

temperature for 20 minutes to form PEI solutions with concentrations of about 4, 8, and 12 wt%. 2, 4, 6 g of PEI was dissolved in 48, 46, 44 g of purified water and stirred at room temperature for 20 min to form PEI solutions with a concentration of about 4, 8, 12 wt%, respectively. 200  $\mu$ l of PEI solution was dropped evenly on the surface of S-CNF-W-CMF. The S-CNF-W-CMF was sandwiched between two filter papers and dried at 70 °C for 15 min to prepare a PEI-S-CNF-W-CMF with a PEI loading weight of 1.0 ( $-\text{NH}_{n1}$ ), 2.0 ( $-\text{NH}_{n2}$ ), 3.0 ( $-\text{NH}_{n3}$ )  $\text{mg}/\text{cm}^2$ , respectively.

The surface potential of the samples was measured using an AFM system (Hitachi, AFM5100N, Japan). The surface and cross-sectional morphologies of the samples were characterized using SEM (Jeol Neoscope JCM-5000). The chemical features were assessed by using ATR-FTIR (SENSOR II, Brook Technology, Germany). K-Alpha XPS (Thermo Fisher Scientific, ESCALAB 250XI+, USA) was used to analyze the surface chemical composition of the samples before and after modification. Contact angle (CA) measurements were performed using a CA measurement system (Ramé-Hart model 500-F1, Ramé-Hart Instrument Co.).

*PVA-CNF-PEO tribolayer:* A suspension composed of PVA, 3% of CNF (based on the dry weight of PVA), and 8% of PEO (based on the total dry weight of PVA and CNF) was used to produce the electrospun webs. The aqueous suspension was added to a 10 mL syringe to form the fluid jet under ambient humidity (45% RH) and 25 °C, using an applied voltage of 30 kV, at a spinning speed of 2 mL/h for 6h.

*Fabrication of the W-TENG unit:* An acrylic sheet with a thickness of 6.0 mm was cut into two pieces of 60  $\times$  60 mm plates to act as the substrate. The PEI-S-CNF-W-CMF film was cut into a 20  $\times$  30 mm and pasted to the sides of the acrylic sheet using conductive copper tape, which

acted as a positive triboelectric material. The PVA–CNF–PEO film was cut into the same size and attached to the sides of the acrylic sheet to act as the negative triboelectric material. PEI–S–CNF–W–CMF and PVA–CNF–PEO were relatively assembled and separated by four springs to form a 2-mm gap. A wire was attached to the component to facilitate current output.

*Fabrication of the G-TENG array:* An acrylic board with a thickness of 3.0 mm was cut into pieces of plates to act as the shell of the system. The acrylic board was also cut and spliced into a grid structure with nine independent spaces, and a high-strength stainless steel ball (Type 304 material, 6.8 g) was placed into each space. Every W-TENG unit was placed in the middle of the two grids, which were jointly sealed and integrated inside the G-TENG array. All W-TENG units were rectified and subsequently connected in parallel.

*Output measurements of the W-TENG unit and G-TENG array:* The open-circuit voltage, short-circuit-transferred charges, and short-circuit current were measured with a Keithley 6514 system electrometer and a data acquisition device (National Instruments, BNC-2120). A digital linear motor (LinMot H01-23 3 86/160) was used to realize the contact and separation cycle with different forces and frequencies. A wave simulation system used a motor of adjustable speed (CX-W4) equipped with a reduction gearbox , which mimicked the water wave motion but under controlled set of frequency.

### **Declaration of Competing Interest**

The authors declare no competing financial interest.

### **Acknowledgements**

This work was supported by the National Key R&D Program of China (2019YFC1905900), the

National Natural Science Foundation of China (31870566), the Jinan Innovation Team (2021GXRC023), and Taishan Scholars Program. OJR and ZD are grateful for the support received from the Canada Excellence Research Chair Program (CERC-2018-00006), the Canada Foundation for Innovation (Project number 38623) and the European Research Council (ERC) under the European Union's Horizon 2020 research and innovation program (grant agreement No 788489).

## References

- [1] F.R. Fan, W. Tang, Z.L.J.A.M. Wang, Flexible nanogenerators for energy harvesting and self - powered electronics, 28 (2016) 4283-4305.
- [2] W. Zhong, L. Xu, H. Wang, D. Li, Z.L.J.N.E. Wang, Stacked pendulum-structured triboelectric nanogenerators for effectively harvesting low-frequency water wave energy, 66 (2019) 104108.
- [3] A. Khaligh, O.C. Onar, Energy harvesting: solar, wind, and ocean energy conversion systems, CRC press 2017.
- [4] Z.L. Wang, T. Jiang, L.J.N.E. Xu, Toward the blue energy dream by triboelectric nanogenerator networks, 39 (2017) 9-23.
- [5] S.P. Beeby, M.J. Tudor, N.J.M.s. White, technology, Energy harvesting vibration sources for microsystems applications, 17 (2006) R175.
- [6] H. Kulah, K.J.I.S.J. Najafi, Energy scavenging from low-frequency vibrations by using frequency up-conversion for wireless sensor applications, 8 (2008) 261-268.
- [7] D. Shen, J.-H. Park, J.H. Noh, S.-Y. Choe, S.-H. Kim, H.C. Wickle III, D.-J.J.S. Kim, a.A. physical, Micromachined PZT cantilever based on SOI structure for low frequency vibration energy harvesting, 154 (2009) 103-108.
- [8] A.J.M.E. Von Jouanne, Harvesting the waves, 128 (2006) 24-27.
- [9] A.J.I.t.o.m. Wolfbrandt, Automated design of a linear generator for wave energy converters-a simplified model, 42 (2006) 1812-1819.
- [10] P. Bai, G. Zhu, Z.-H. Lin, Q. Jing, J. Chen, G. Zhang, J. Ma, Z.L.J.A.n. Wang, Integrated multilayered triboelectric nanogenerator for harvesting biomechanical energy from human motions, 7 (2013) 3713-3719.
- [11] F.-R. Fan, Z.-Q. Tian, Z.L.J.N.e. Wang, Flexible triboelectric generator, 1 (2012) 328-334.

- [12] G. Zhu, Z.-H. Lin, Q. Jing, P. Bai, C. Pan, Y. Yang, Y. Zhou, Z.L.J.N.I. Wang, Toward large-scale energy harvesting by a nanoparticle-enhanced triboelectric nanogenerator, 13 (2013) 847-853.
- [13] Y. Liu, W. Liu, Z. Wang, W. He, Q. Tang, Y. Xi, X. Wang, H. Guo, C.J.N.c. Hu, Quantifying contact status and the air-breakdown model of charge-excitation triboelectric nanogenerators to maximize charge density, 11 (2020) 1-8.
- [14] Z.L.J.N.E. Wang, On the first principle theory of nanogenerators from Maxwell's equations, 68 (2020) 104272.
- [15] G. Chen, Y. Li, M. Bick, J.J.C.R. Chen, Smart textiles for electricity generation, 120 (2020) 3668-3720.
- [16] A. Yu, Y. Zhu, W. Wang, J.J.A.F.M. Zhai, Progress in triboelectric materials: toward high performance and widespread applications, 29 (2019) 1900098.
- [17] N. Zhang, C. Tao, X. Fan, J.J.J.o.M.R. Chen, Progress in triboelectric nanogenerators as self-powered smart sensors, 32 (2017) 1628-1646.
- [18] Z.L.J.M.T. Wang, On Maxwell's displacement current for energy and sensors: the origin of nanogenerators, 20 (2017) 74-82.
- [19] J. Shao, M. Willatzen, T. Jiang, W. Tang, X. Chen, J. Wang, Z.L.J.N.E. Wang, Quantifying the power output and structural Fig.-of-merits of triboelectric nanogenerators in a charging system starting from the Maxwell's displacement current, 59 (2019) 380-389.
- [20] H.-Y. Mi, X. Jing, Q. Zheng, L. Fang, H.-X. Huang, L.-S. Turng, S.J.N.E. Gong, High-performance flexible triboelectric nanogenerator based on porous aerogels and electrospun nanofibers for energy harvesting and sensitive self-powered sensing, 48 (2018) 327-336.
- [21] H.-Y. Mi, X. Jing, M.A.B. Meador, H. Guo, L.-S. Turng, S.J.A.a.m. Gong, interfaces, Triboelectric nanogenerators made of porous polyamide nanofiber mats and polyimide aerogel film: output optimization and performance in circuits, 10 (2018) 30596-30606.
- [22] S. Chen, J. Jiang, F. Xu, S.J.N.E. Gong, Crepe cellulose paper and nitrocellulose membrane-based triboelectric nanogenerators for energy harvesting and self-powered human-machine interaction, 61 (2019) 69-77.
- [23] C. Wu, T.W. Kima, S. Sung, J.H. Park, F.J.N.E. Li, Ultrasoft and cuttable paper-based triboelectric nanogenerators for mechanical energy harvesting, 44 (2018) 279-287.
- [24] C. Yao, X. Yin, Y. Yu, Z. Cai, X.J.A.F.M. Wang, Chemically functionalized natural cellulose materials for effective triboelectric nanogenerator development, 27 (2017) 1700794.
- [25] Y. Yu, Z. Li, Y. Wang, S. Gong, X.J.A.M. Wang, Sequential infiltration synthesis of doped polymer films with tunable electrical properties for efficient triboelectric nanogenerator development, 27 (2015) 4938-4944.
- [26] C. Zhang, J. Mo, Q. Fu, Y. Liu, S. Wang, S.J.N.E. Nie, Wood-cellulose-fiber-based functional

- materials for triboelectric nanogenerators, 81 (2021) 105637.
- [27] Z. Li, J. Chen, J. Yang, Y. Su, X. Fan, Y. Wu, C. Yu, Z.L.J.E. Wang, E. Science,  $\beta$ -cyclodextrin enhanced triboelectrification for self-powered phenol detection and electrochemical degradation, 8 (2015) 887-896.
- [28] G.Q. Gu, C.B. Han, C.X. Lu, C. He, T. Jiang, Z.L. Gao, C.J. Li, Z.L.J.A.n. Wang, Triboelectric nanogenerator enhanced nanofiber air filters for efficient particulate matter removal, 11 (2017) 6211-6217.
- [29] M. Zhang, M. Zhao, M. Jian, C. Wang, A. Yu, Z. Yin, X. Liang, H. Wang, K. Xia, X.J.M. Liang, Printable smart pattern for multifunctional energy-management e-textile, 1 (2019) 168-179.
- [30] X. Pu, M. Liu, X. Chen, J. Sun, C. Du, Y. Zhang, J. Zhai, W. Hu, Z.L.J.S.a. Wang, Ultrastretchable, transparent triboelectric nanogenerator as electronic skin for biomechanical energy harvesting and tactile sensing, 3 (2017) e1700015.
- [31] J. Chen, Z.L.J.J. Wang, Reviving vibration energy harvesting and self-powered sensing by a triboelectric nanogenerator, 1 (2017) 480-521.
- [32] Y. Zhou, W. Deng, J. Xu, J.J.C.R.P.S. Chen, Engineering materials at the nanoscale for triboelectric nanogenerators, 1 (2020) 100142.
- [33] H. Zhang, Y. Yang, Y. Su, J. Chen, K. Adams, S. Lee, C. Hu, Z.L.J.A.F.M. Wang, Triboelectric nanogenerator for harvesting vibration energy in full space and as self - powered acceleration sensor, 24 (2014) 1401-1407.
- [34] J. Yang, J. Chen, Y. Liu, W. Yang, Y. Su, Z.L.J.A.n. Wang, Triboelectrification-based organic film nanogenerator for acoustic energy harvesting and self-powered active acoustic sensing, 8 (2014) 2649-2657.
- [35] Y. Yang, H. Zhang, R. Liu, X. Wen, T.C. Hou, Z.L.J.A.E.M. Wang, Fully enclosed triboelectric nanogenerators for applications in water and harsh environments, 3 (2013) 1563-1568.
- [36] X. Wang, S. Niu, Y. Yin, F. Yi, Z. You, Z.L.J.A.E.M. Wang, Triboelectric nanogenerator based on fully enclosed rolling spherical structure for harvesting low - frequency water wave energy, 5 (2015) 1501467.
- [37] L. Xu, T. Jiang, P. Lin, J.J. Shao, C. He, W. Zhong, X.Y. Chen, Z.L.J.A.n. Wang, Coupled triboelectric nanogenerator networks for efficient water wave energy harvesting, 12 (2018) 1849-1858.
- [38] H.S. Wang, C.K. Jeong, M.-H. Seo, D.J. Joe, J.H. Han, J.-B. Yoon, K.J.J.N.E. Lee, Performance-enhanced triboelectric nanogenerator enabled by wafer-scale nanogrates of multistep pattern downscaling, 35 (2017) 415-423.
- [39] S.K. Paul, P.J.G.J.o.F.S.M. Chowdhury, Strategies for managing the impacts of disruptions during COVID-19: an example of toilet paper, 21 (2020) 283-293.
- [40] E. van der Roest, M. van der Spek, A. Ramirez, B. Van Der Zwaan, G.J.E.T. Rothenberg,

Converting Waste Toilet Paper into Electricity: A First - Stage Technoeconomic Feasibility Study, 5 (2017) 2189-2197.

[41] H. Kishino, K. Hanyu, M. Yamashita, C.J.R. Hayashi, Conservation, Recycling, Recycling and consumption in Germany and Japan: a case of toilet paper, 26 (1999) 189-215.

[42] S. Li, Z. Wu, G.J.C. Liu, Degradation kinetics of toilet paper fiber during wastewater treatment: Effects of solid retention time and microbial community, 225 (2019) 915-926.

[43] X. Wen, W. Yang, Q. Jing, Z.L.J.A.n. Wang, Harvesting broadband kinetic impact energy from mechanical triggering/vibration and water waves, 8 (2014) 7405-7412.

[44] H. Kang, C. Zhao, J. Huang, D.H. Ho, Y.T. Megra, J.W. Suk, J. Sun, Z.L. Wang, Q. Sun, J.H.J.A.F.M. Cho, Fingerprint - inspired conducting hierarchical wrinkles for energy - harvesting E - skin, 29 (2019) 1903580.

[45] B. Yu, H. Yu, T. Huang, H. Wang, M.J.N.E. Zhu, A biomimetic nanofiber-based triboelectric nanogenerator with an ultrahigh transfer charge density, 48 (2018) 464-470.

[46] X. He, H. Zou, Z. Geng, X. Wang, W. Ding, F. Hu, Y. Zi, C. Xu, S.L. Zhang, H.J.A.F.M. Yu, A hierarchically nanostructured cellulose fiber - based triboelectric nanogenerator for self - powered healthcare products, 28 (2018) 1805540.

[47] Y. Mao, N. Zhang, Y. Tang, M. Wang, M. Chao, E.J.N. Liang, A paper triboelectric nanogenerator for self-powered electronic systems, 9 (2017) 14499-14505.

[48] K.Y. Lee, J. Chun, J.H. Lee, K.N. Kim, N.R. Kang, J.Y. Kim, M.H. Kim, K.S. Shin, M.K. Gupta, J.M.J.A.m. Baik, Hydrophobic sponge structure - based triboelectric nanogenerator, 26 (2014) 5037-5042.

[49] C. Zhao, H. Feng, L. Zhang, Z. Li, Y. Zou, P. Tan, H. Ouyang, D. Jiang, M. Yu, C.J.A.F.M. Wang, Highly efficient in vivo cancer therapy by an implantable magnet triboelectric nanogenerator, 29 (2019) 1808640.

[50] X. Zhang, L. Chen, Y. Jiang, W. Lim, S.J.C.o.M. Soh, Rationalizing the triboelectric series of polymers, 31 (2019) 1473-1478.

[51] Z.L. Wang, A.C.J.M.T. Wang, On the origin of contact-electrification, 30 (2019) 34-51.

[52] C. Xu, Y. Zi, A.C. Wang, H. Zou, Y. Dai, X. He, P. Wang, Y.C. Wang, P. Feng, D.J.A.M. Li, On the electron - transfer mechanism in the contact - electrification effect, 30 (2018) 1706790.

[53] H.Y. Li, L. Su, S.Y. Kuang, C.F. Pan, G. Zhu, Z.L.J.A.F.M. Wang, Significant enhancement of triboelectric charge density by fluorinated surface modification in nanoscale for converting mechanical energy, 25 (2015) 5691-5697.

[54] M. Ma, R.M.J.C.o.i.c. Hill, i. science, Superhydrophobic surfaces, 11 (2006) 193-202.

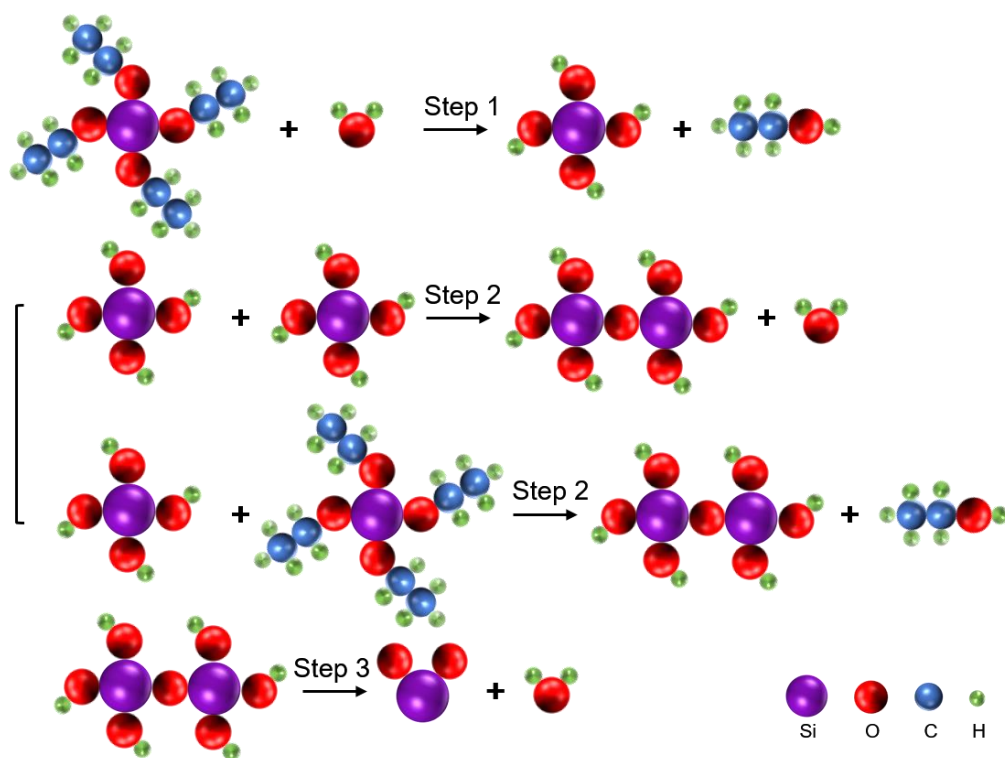


**Fig. S1.** Formation mechanism of SiO<sub>2</sub>

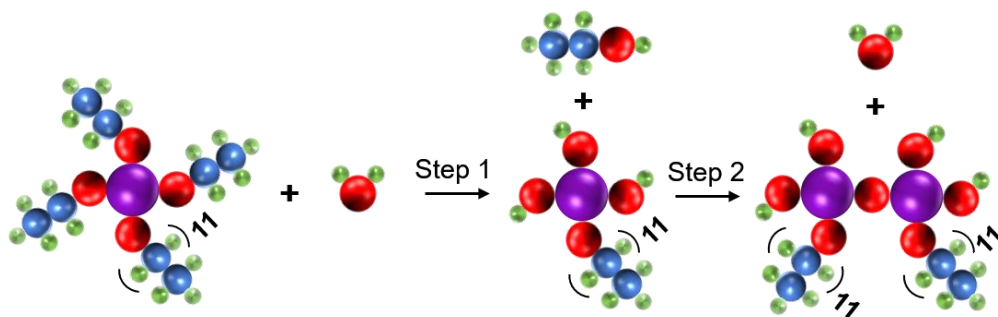


**Fig. S2.** Hydrolysis mechanism of CH<sub>3</sub>[CH<sub>2</sub>]<sub>11</sub>Si[OCH<sub>2</sub>CH<sub>3</sub>]<sub>3</sub>

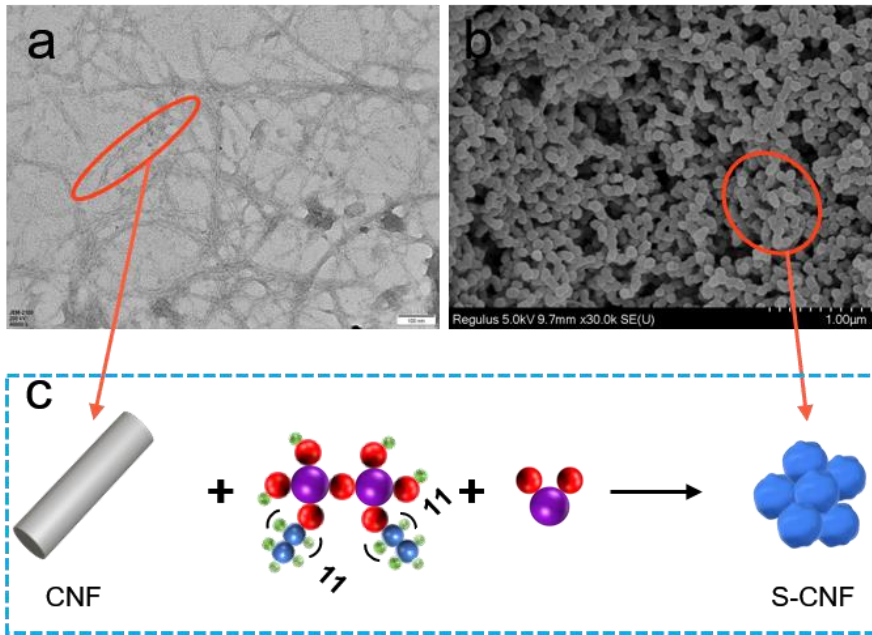


**Fig. S3.** S-CNF before and after silanization modification. (a) TEM of CNF, (b) SEM of S-CNF, (c) Formation mechanism of S-CNF

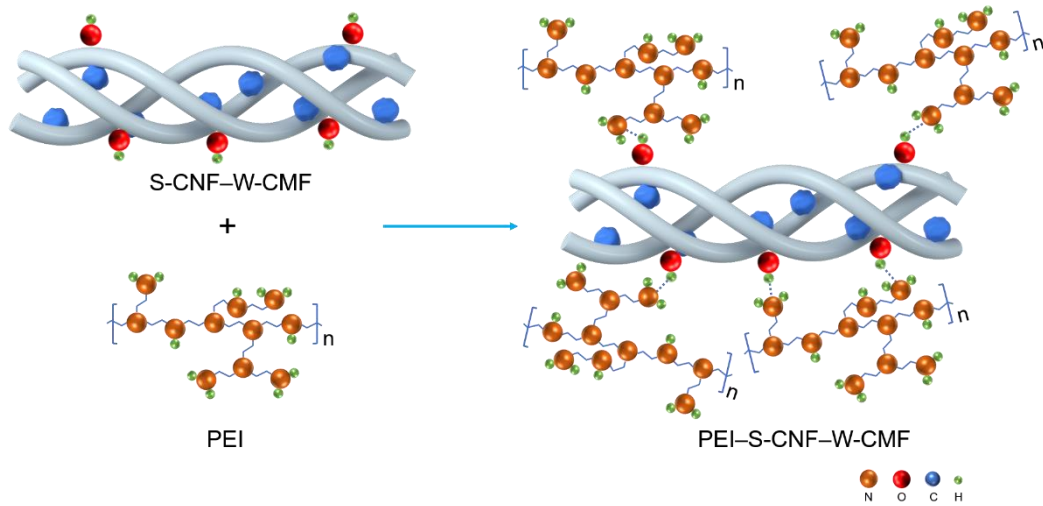


**Fig. S4.** Mechanism of PEI reaction

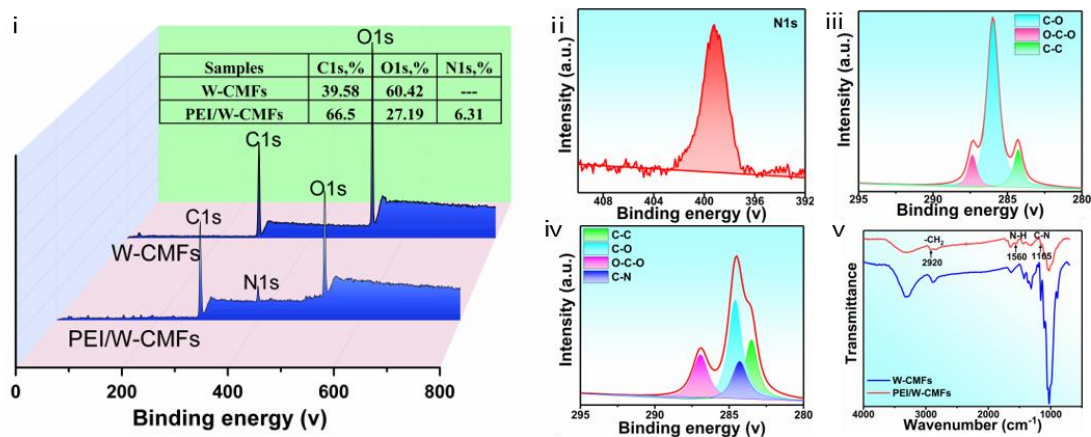


**Fig. S5.** X-ray photoelectron spectroscopy (XPS) spectra of (i) W-CMF and PEI-W-CMF, (ii) N 1 s of PEI-W-CMF, (iii) C 1 s of W-CMF, (iv) C 1 s of PEI-W-CMF, and (v) Fourier transform infrared spectroscopy (FTIR) of W-CMF and PEI-W-CMF.

Compared to the energy peaks of C 1 s and O 1 s of the W-CMF, the N 1 s peak of the PEI-W-CMF appears, with the nitrogen content reaching  $\sim 6.3\%$  (i and ii). To further understand the bonding form between atoms, the binding energy peaks are analyzed. Peaks at 283.4, 284.5, and 286.9 eV were observed, corresponding to the C-C, C-O, and O-C-O structures in cellulose (iii), and a new C-N binding energy peak of PEI-W-CMF appears at 284.2 eV (iv). Compared with W-CMF, the absorption peaks at 1165, 1560, and 2920  $\text{cm}^{-1}$  are observed in PEI-W-CMF, which are attributed to the vibration of N-H, C-N, and -CH<sub>2</sub> (v).

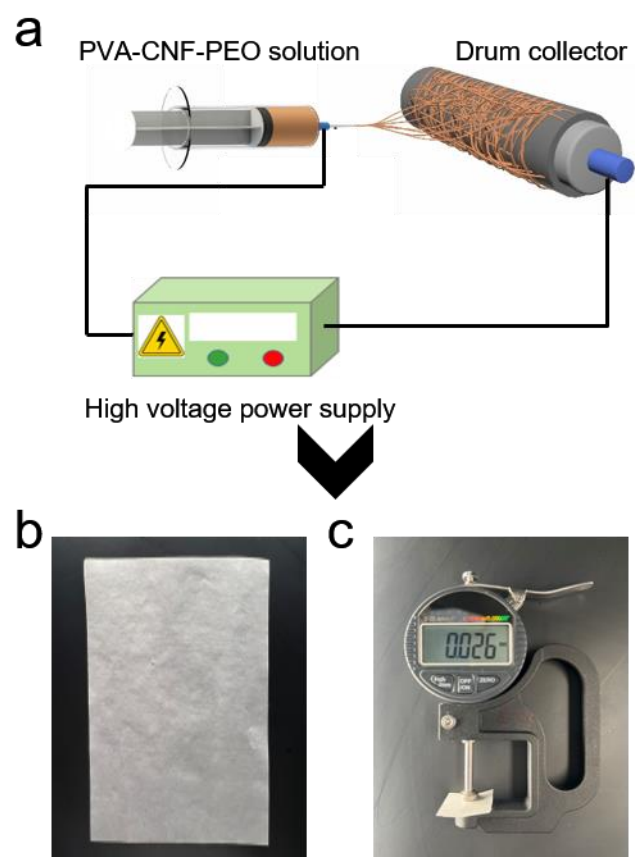


**Fig. S6.** (a) Schematic of fabricating PVA–CNF–PEO film by electrospinning. (b) Physical photo and (c) thickness of PVA–CNF–PEO membrane.

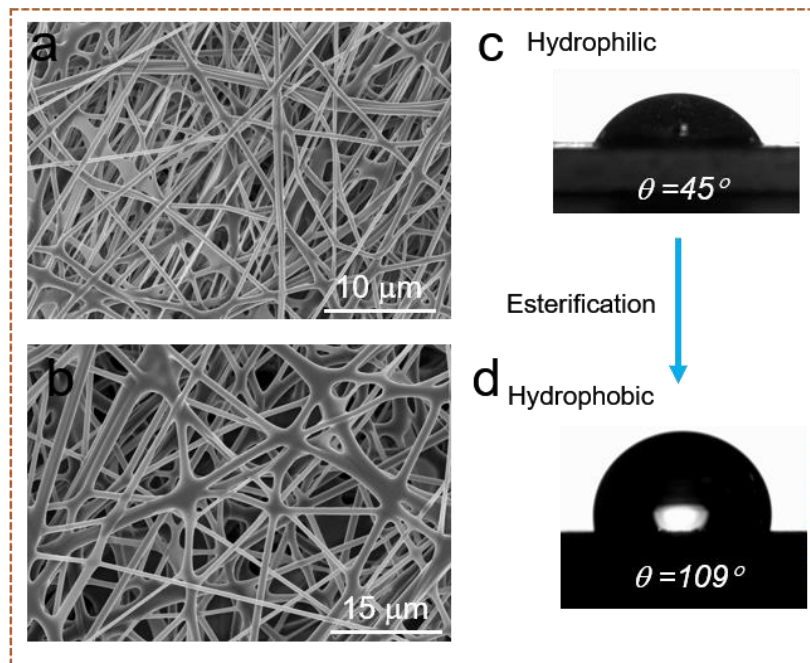


**Fig. S7.** SEM topography of (a) PVA-CNF-PEO and (b) esterified PVA-CNF-PEO. Contact angle of (c) PVA-CNF-PEO and (d) esterified PVA-CNF-PEO at 2 min.

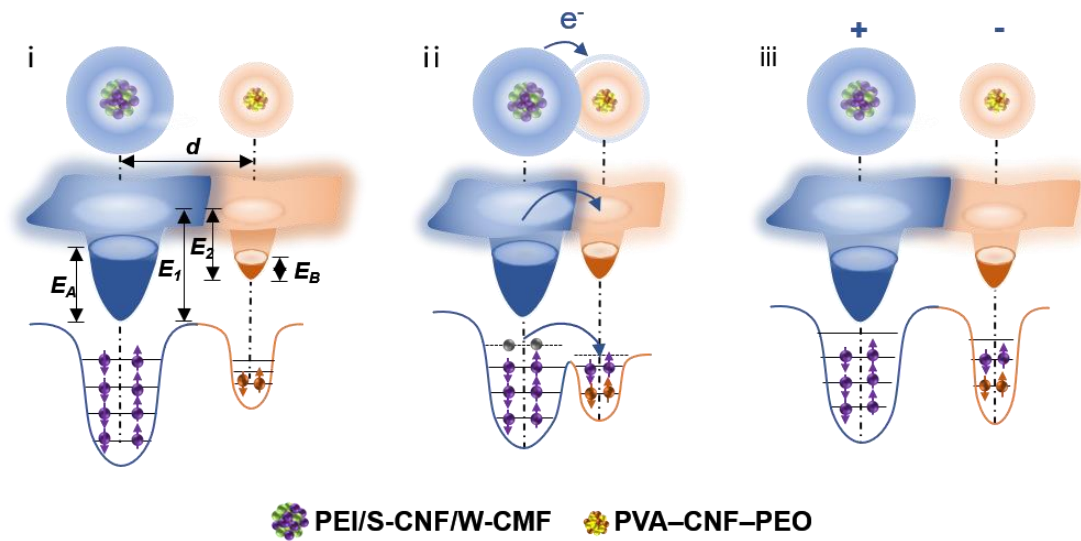


**Fig. S8.** Electron cloud model describing the triboelectric process of W-TENG.

When the atoms of PEI-S-CNF-W-CMF and PVA-CNF-PEO are far apart, their electron clouds are not in contact, and electrons are tightly bound in atomic orbitals with a high escape energy barrier (i). Triggered by external force, the atoms of PEI-S-CNF-W-CMF and PVA-CNF-PEO gradually become closer, and then reach the interatomic repulsion region, where the electron clouds overlap. Further, interatomic barrier is significantly reduced (ii). Consequently, some high-energy electrons in PEI-S-CNF-W-CMF can easily overcome the reduced potential barrier and transfer to PVA-CNF-PEO, eventually reaching equilibrium. As the atoms of PEI-S-CNF-W-CMF and PVA-CNF-PEO are completely out of contact, the transferred electrons and holes are in the form of electrostatic charges retained on the surfaces of PEI-S-CNF-W-CMF and PVA-CNF-PEO (iii).

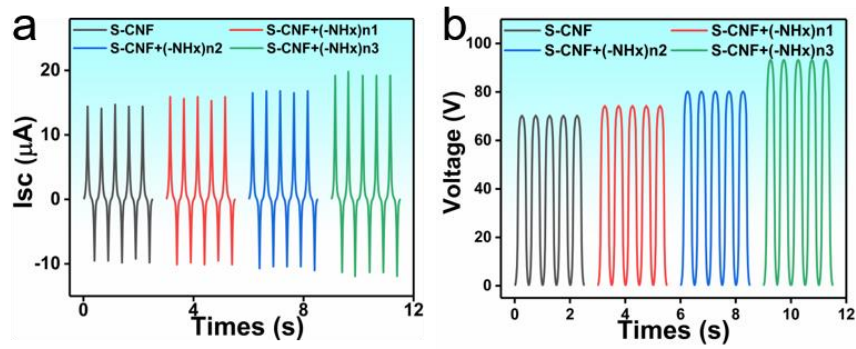


**Fig. S9.** (a) Output current, and (b) voltage of the W-TENG based on PEI-S-CNFs-W-CMFs with different amounts of  $-NH_x$ .

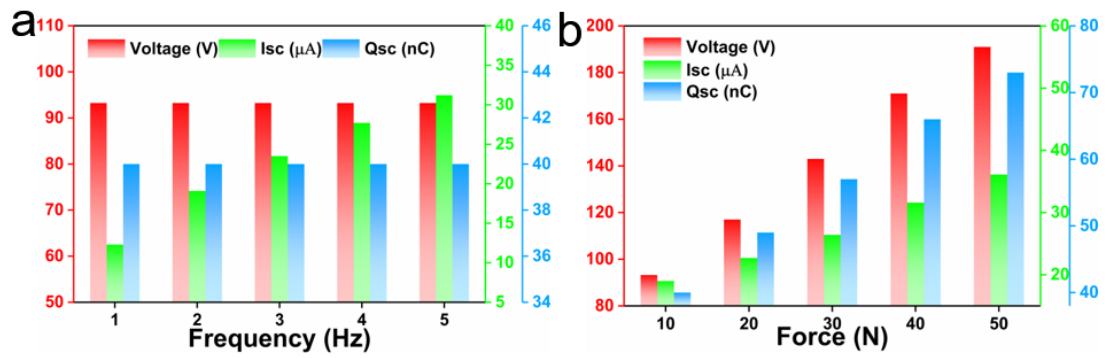


**Fig. S10.** Output voltage, current, and transferred charges of the as-fabricated W-TENG (a) at various excitation frequencies ranging from 1 to 5 Hz, and (b) at different forces ranging from 10 to 50 N.